

Inception of Regular Valley Spacing in Fluvial Landscapes: A Linear Stability Analysis

**Shashank Kumar Anand¹, Sara Bonetti², Carlo Camporeale³, and Amilcare
Porporato^{1,4}**

¹Department of Civil and Environmental Engineering, Princeton University, USA

²Soil Physics and Land Management Group, Wageningen University, The Netherlands

³Department of Environment, Land and Infrastructure Engineering, Politecnico di Torino, Italy

⁴High Meadows Environmental Institute, Princeton University, USA

Key Points:

- The linear stability analysis quantifies the critical erosion limit for incipient channelization.
- Incipient valley spacing widens for higher values of the exponent that couples fluvial erosion and the specific drainage area.
- Results from the stability analysis conform with the numerical simulations and data from a natural landscape.

Corresponding author: Amilcare Porporato, aporpora@princeton.edu

Abstract

Incipient channelization in mountainous landscapes is often associated with the presence of first-order valleys at a regular wavelength under diverse hydroclimatic forcings. Here we provide a formal linear stability analysis of a landscape evolution model in detachment-limited erosion conditions to quantify the impact of the erosion law on the regular valley formation. The linear stability analysis is conducted for the unchannelized hillslope solutions along a long mountain ridge, where the perturbed equations constitute a third-order differential eigenvalue problem. The solutions to the posed eigenvalue problem are obtained by a spectral Galerkin technique with numerical quadrature. Results reveal the dependence of the erosion threshold and the emergent ridge/valley wavelength on the exponents in the power-law scaling coupling fluvial erosion with specific drainage area (m) and local slope (n). As the exponent m increases for a fixed n , the emergent valley spacing expands and the erosion limit for the first channel instability declines. Conversely, the erosion threshold for the first channelization rises with an increase in n at a particular value of m . We also show that predictions of the stability analysis conform with numerical simulations for different degrees of nonlinearity in the erosion mechanism and agree well with topographic data of a natural landscape.

Plain Language Summary

Landscapes tend to exhibit equally spaced valleys at the onset of channelization, which occurs when the fluvial erosion overcomes the smoothing effects of the hillslope processes. To theoretically predict the conditions for the first channelization, we study the growth of very small disturbances added to the landscape forms with no channels. The results indicate a minimum erosion limit below which no valleys are present. This critical erosion limit and the emergent valley spacing are determined by the relation between the specific upstream area and the topographic slope in fluvial erosion law. The theoretical findings are in good agreement with the numerical simulations and the topographic data from a natural landscape.

1 Introduction

The relative strength of diffusive soil creep and fluvial erosion leads to a distinctive spatial arrangement of interlocked ridges and valleys (Kirkby, 1971; Willgoose et al., 1991; Rodriguez-Iturbe & Rinaldo, 2001; Birnir et al., 2001; Roering, 2008; Hancock et al., 2010; Fowler, 2011; Singh et al., 2015; Bonetti et al., 2020). A crucial juncture of this balance controlling hillslope morphology occurs when erosion is just high enough to overcome the effect of soil creep and starts carving the surface, thereby leading to the formation of first-order valleys in the landscape. Historically, the presence of regularly-spaced valleys along mountainous ridges has stimulated efforts to understand the emergence of such a deterministic behavior of the channelization onset (Gilbert & Dutton, 1880; Shaler, 1899; Hallet, 1990; Talling et al., 1997; Parker & Izumi, 2000; Allen, 2005; Perron, Kirchner, & Dietrich, 2008).

The results from topographic observations in mountainous landscapes with distinct vegetation cover and climate conditions indicate that the channel initiation tends to occur at a characteristic spatial scale (Perron, Dietrich, & Kirchner, 2008; Perron et al., 2009). Even for well-developed channelization regimes with several length scales, in the power spectrum of the landscape elevation a ‘typical’ wavenumber demarcates around which most of the energy content is concentrated with a sharp (and power-law) decline in the energy at high wavenumbers (Hooshyar et al., 2021; Porporato, 2022). These observations lead to an interesting set of questions regarding the role of the feedback in landscape-evolution processes in determining the emerging channelization mode as well as the intensity of fluvial erosion needed for the first dissection of the landscape at that scale. A

quantitative link between this spectral signature of channelization and the form of the erosion laws has not yet been completely established. The present work offers a contribution toward this goal. We focus here on a minimalist landscape evolution model (LEM) (Bonetti et al., 2020) that contains the least amount of complexity to describe the regularly-spaced channel initiation and pinpoint the corresponding nonlinear feedbacks that induce this phenomenon over geological time scales. While comprehensive landscape evolution modeling studies (e.g., Collins et al. (2004); Van De Wiel et al. (2007); Attal et al. (2008); Coulthard et al. (2013)), including spatiotemporal heterogeneity and parametrization for a wide array of geomorphological processes, are a powerful tool to provide the linkages between distinct processes and the consequent morphological evolution, they tend to be too involved to allow for theoretical developments that can help isolate the underlying basic mechanisms driving the emergence of ubiquitous landscape patterns.

1.1 Brief Literature Review

Before starting our review of the investigations of landscape stability, it is useful to orient the reader on the extensive literature on channel formation in natural landscapes and how different formulations vary in their description of the coupled water and sediment dynamics. Regarding surface water modeling, the more comprehensive approaches adopt the full-version of shallow-water equations primarily in steady-state conditions, thereby including the effect of gravity, pressure, and inertial forces on the surface water flow (Chen et al., 2014). The next category of approximation dismisses the inertial effects over long time scales (Leopold & Maddock, 1953; Weinmann & Laurenson, 1979; Smith, 2010). The minimalist form of water transport assumes a steady-state flow along the topographic gradient or normal-flow hypothesis. Efforts by Gallant and Hutchinson (2011), Bonetti et al. (2018) and Porporato (2022) established that this water transport formalism is analogous to the mathematical equation of the specific drainage area, a , for the constant flow speed of the water.

Regarding the modeling of long-term fluvial erosion processes, LEMs are typically considered either in the transport-limited (TL) or the detachment-limited (DL) conditions. Some research works have also considered intermediate conditions between these two regimes (Davy & Lague, 2009; Pelletier, 2012). Under the TL approximation, the fluvial erosion assumes the form of the divergence of the sediment flux, which in turn, is related to the shear stress of the surface flow (Willgoose et al., 1991; G. E. Tucker & Bras, 1998; Hergarten, 2020). The erosion flux is directly related to the shear stress by flowing water in the DL approximation with the underlying assumption that the surface resistance to incision is the restricting factor for the erosion rate rather than the hauling capacity of the flow to transport the eroded material (Ahnert, 1987; Howard, 1994). Hence, the mathematical form of fluvial erosion becomes a sink term in the LEM with a power-law relation to the specific drainage area and local slope.

Within this context, the pioneering work by Smith and Bretherton (1972) provided the first stability analysis of symmetric hillslopes to small lateral perturbations employing a continuous model for water under normal-flow hypothesis and sediment fluxes for TL erosion conditions. This study showed that the concave-up portions of the hillslope are unstable to lateral perturbations. Nevertheless, the analysis did not predict a characteristic wavelength for the channel instability with an unbound increase in the growth rate for high-frequency perturbations. Whereas this shortcoming has been attributed to the use of normal-flow approximation for the water continuity equation (Loewenherz-Lawrence, 1994; Smith, 2010; Fowler, 2011), here we show that the stability analysis considering minimalist flow approximation with soil creep and DL erosion condition leads to a finite channelization mode at a critical threshold of the fluvial erosion. These findings suggest that the assumption of constant coefficients in the perturbed governing equations in the work of Smith and Bretherton (1972) could be related to the lack of wavelength selection, as also noted by Fowler (2011).

Izumi and Parker (1995) and Izumi and Parker (2000) performed a linear stability analysis of the coupled system of shallow water flow in quasi-steady conditions with the DL approximation for the fluvial erosion. In particular, Izumi and Parker (1995) described channelization as the upstream-driven process over an assumed tilted planar surface, where the channels initiate as the surface discharge reaches a critical threshold. The case of downstream-driven erosion over a steady concave-down erodible surface was analyzed by Izumi and Parker (2000). They focused on deriving finite valley spacing for the channel initiation but considered constrained assumptions regarding perturbation structures and the flow boundary conditions. Additionally, Smith (2010) presented a detailed mathematical framework depicting the channel formation with the quasi-steady flow down the energy-surface gradient in the TL and DL erosion environments. The initial hillslope was assumed to be a steady planar profile over which small perturbations could evolve.

All the previous theoretical contributions considered perturbations on somewhat artificial surfaces. The simple hillslope forms used in these studies facilitated analytical tractability to determine the appearance of well-defined channels, but they are not necessarily steady-state solutions of LEMs and therefore have limited bearing to natural landscape morphologies. In this regard, a more realistic starting point to investigate the conditions of valley formation was pursued by Perron, Dietrich, and Kirchner (2008) and Perron et al. (2009), who described the evenly-spaced valley formation for the numerical solutions of LEM under the DL fluvial erosion and drainage area field as a proxy for the water flux. Using numerical simulations, they showed that the relative timescale of fluvial erosion compared to soil creep controls the valley spacing scale. However, these analyses did not carry out a formal stability analysis and were limited to numerical simulations.

Employing unchannelized solutions of LEMs with specific boundary conditions in a linear stability formulation would help to formulate precisely the criteria for the channelization onset. A preliminary analysis along these lines was conducted by Bonetti et al. (2020) using a minimalist DL-LEM for the special case of unitary exponents of the drainage area and topographic slope. However, a more complete stability analysis that includes the effect of the nonlinear scaling exponents in the erosion on the channel formation for base-state solutions of the minimalist LEM is still missing and motivates the work here.

1.2 Goal of This Contribution

Within the context outlined before, in this paper we focus on a minimalist LEM in DL conditions and normal-flow approximation for the water flow. We conduct a linear stability analysis of the unchannelized solutions of the governing equations to identify the conditions under which an initially smooth surface assumes a morphology similar to observed regularly-spaced first-order drainage basins. The DL erosion model is adopted based on the arguments that the bed erosion for the first channelization over the hillslope and low-order valleys is bounded by the erosive power/shear stress of the overland flow rather than the flow capacity to transport the eroded sediments (Howard, 1994; Izumi & Parker, 1995).

We consider two symmetric hillslopes along a linear ridgeline as an idealization of a long mountain ridge in a natural landscape (see Section 3.4) to derive unchannelized base-state solutions of the governing equations (Bonetti et al., 2019, 2020; Anand et al., 2020). Differently from previous contributions, the mathematical forms of the unchannelized solutions are obtained by applying the boundary conditions of water and sediment fluxes in the governing equations and solving for the steady-state (the so-called base-state profile) rather than assuming an arbitrary initial form of the erodable surface. Since the solutions are analytically attainable only for m and n equal to 1 (see equation (12)),

we adopt a numerical procedure here to compute base-state hillslope profiles for generic values of m and n .

The stability problem is solved by utilizing a spectral technique based on the Galerkin projection with numerical quadrature (Canuto et al., 2006), which has been shown to be particularly performant and well suited for morphological problems (Camporeale et al., 2012; Camporeale & Ridolfi, 2012; Camporeale, 2015). Employing this strategy, the impact of nonlinearities present in the erosion law on the hillslope stability and the incipient channelization is discussed as erosion gets intensified with respect to soil creep. The predictions of the stability analysis are compared with the numerical simulations in a long rectangular domain for different values of the exponents and also with the topographic data of a natural landscape. The obtained results show that the regularly-spaced valleys emerge at a certain proportion of fluvial erosion and soil creep. From the water-flow modeling perspective, our results also show that the minimalist normal-flow hypothesis leads to a spatial wavelength preference on the channelization onset under the action of DL erosion and soil creep.

The article is structured as follows. In section 2, we present the coupled governing equations of water and surface elevation in the DL framework, along with domain geometry and boundary conditions used in this study. We further derive the linearized perturbed equations that are recast in terms of a third-order differential eigenvalue problem. In section 3, the results from the linear stability analysis are discussed. The presented method is verified for the special case of unitary exponents in the model. We show the control of the power-law exponents of the specific drainage area and slope in the erosion term on the threshold erosion rate for first channelization and incipient valley spacing. A comparison between stability analysis predictions and results from numerical simulations is carried out for different values of exponents m and n . We finally show the findings of the stability analysis using the topographic data from a natural landscape.

2 Linear Stability Analysis

This section presents the mathematical equations for the minimalist LEM in DL conditions for fluvial erosion. We define the unchannelized base-state solutions for two symmetric and opposite hillslopes along a long ridge by imposing zero water and sediment flux boundary conditions at the ridgeline and fixed-level boundary conditions at the hillslope bases. The stability problem is posed by assuming weak perturbations over the featureless base-state solutions. All arbitrary spatial perturbations are assumed to have very small amplitude compared to the unchannelized solutions, so non-linear (higher-order) interactions do not remain relevant in this regime. Employing normal-mode linear stability analysis, the perturbed governing equations in a linearized form are obtained along with imposed homogeneous boundary conditions.

2.1 Governing Equations

The coupled dynamics of the landscape elevation and surface water fields can be written in general as

$$\frac{\partial z}{\partial t} = U - \nabla \cdot \mathbf{f}_c - \nabla \cdot \mathbf{f}_e, \quad (1)$$

$$\frac{\partial h}{\partial t} = R - \nabla \cdot (q\mathbf{n}). \quad (2)$$

Equation (1) describes the temporal evolution of the elevation field z under the action of tectonic uplift U , sediment flux due to soil creep \mathbf{f}_c , and the flux transported due to fluvial erosion, \mathbf{f}_e . Soil creep is a term used to represent a combined effect of various biophysical processes that result in the slow movement of soil over the hillslope. Surface and subsurface processes inducing this movement include animal burrowing, falling trees, wet-

ting/drying of the upper soil layer, and freezing/thawing cycle of the pore water in the subsurface (Carson & Kirkby, 1972; Gabet et al., 2003). The combined effect of these movements smooths the topography so that the downslope flux can be written as a diffusion term in the average sense, $\mathbf{f}_e = -D_c \nabla z$, where D_c is a coefficient based on combined efficiency of different soil creep processes (Culling, 1963). In the DL approximation, the fluvial erosion flux is assumed proportional to the shear stress by the flowing runoff over the surface as $\nabla \cdot \mathbf{f}_e = K'_e q^m |\nabla z|^n$, where K'_e is an erosion coefficient, q is the specific runoff or the surface flow rate, and m and n are the model exponents (Howard, 1994; Whipple & Tucker, 1999; G. E. Tucker & Hancock, 2010).

In equation (2), R represents a runoff-producing rainfall rate, i.e., the amount of precipitated water contributing to runoff production q in the direction of \mathbf{n} . Under the quasi-steady-state approximation ($\partial h / \partial t = 0$), with water flowing at a constant speed in the direction of steepest descent of the topographic surface ($\mathbf{n} = -\nabla z / |\nabla z|$) and a time-averaged runoff-producing rainfall rate R_0 , the water discharge q is proportional to the specific drainage area $a (= q / R_0)$. As a result, equation (2) becomes the governing equation for the specific drainage area (Bonetti et al., 2020; Porporato, 2022). Employing this proportionality between q and a , the erosion flux is modified as $\nabla \cdot \mathbf{f}_e = K_e a^m |\nabla z|^n$, where $K_e = K'_e R_0^m$.

Under these conditions, equations (1) and (2) get simplified as

$$\frac{\partial z}{\partial t} = D_c \nabla^2 z - K_e a^m |\nabla z|^n + U, \quad (3)$$

$$-\nabla \cdot \left(a \frac{\nabla z}{|\nabla z|} \right) = 1. \quad (4)$$

Through the coupling between a and z , the minimalist LEM, given by the system of equations (3) and (4), captures the essential feedbacks and dynamics of landscapes evolving over long time scales. Fluvial erosion and soil creep act as sink and diffusion terms in equation (3), respectively. Erosion excavates sediment at locations where the accumulation of the specific drainage area is high. This yields a higher surface gradient at those locations with a further increase in a , thus enforcing the increased erosion and flow accumulation again. This feedback loop between the emerging topography and the accumulated specific drainage area can carve a preferential path over time if the surface smoothing effect by the creep diffusion is not sufficient with the progression of a landscape from a smooth topography towards a more dissected one.

For a domain with characteristic length l_x , equations (3) and (4) can be non-dimensionalized to derive a dimensionless quantity

$$\mathcal{C}_{\mathcal{I}} = \frac{K_e l_x^{m+n}}{D_c^n U^{1-n}}, \quad (5)$$

which determines the relative impact of creep, erosion, and uplift on the first channelization and incipient valley spacing. An increase in $\mathcal{C}_{\mathcal{I}}$ (e.g., increased rainfall, declined efficiency of the soil creep, reduced resistance to the fluvial erosion) characterizes the tendency of the landscape to branch and form channels and has been therefore called ‘channelization index’ by Bonetti et al. (2020).

2.2 1D Base-State Morphology

The landscape geometry considered here consists of two opposite and symmetric hillslopes along a linear ridge with zero water and sediment flux at the ridgeline and a fixed-level hillslope base as boundary conditions. These conditions are consistent with those adopted in earlier studies on the analysis of 1D hillslope morphology (Smith & Bretherton, 1972; Loewenherz, 1991; Bonetti et al., 2019). The mathematical form of unchanneled solutions at steady-state can be obtained by using boundary conditions in equations (3) and (4) for the 1D transect.

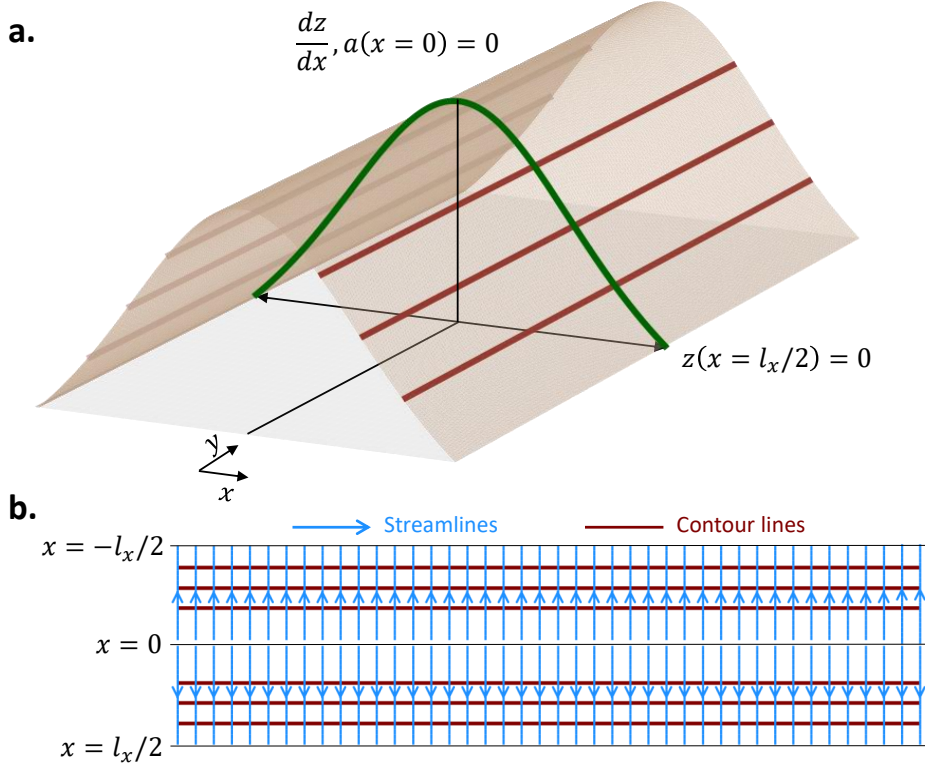


Figure 1. Schematic diagram showing the domain geometry and imposed boundary conditions to compute the unchanneled base-state solutions. (a): A representative 3D steady-state profile is shown, where x -axis points in the direction along the hillslope and y -axis denotes the ridgeline direction normal to the hillslope. The presence of a ridgeline/drainage divide in the center of the domain ensures zero water and sediment flux boundary conditions at $x = 0$. The hillslope baseline is taken fixed at $x = \pm l_x/2$ with zero elevation as the reference level. The green curve shows the unchanneled cross-section profile with l_x as the characteristic length-scale of the domain. (b): The horizontal projection of the landscape is shown with streamlines (in blue) perpendicular to the projected contour lines (in brown).

As shown in figure 1(a), the x -axis points in the direction along the hillslope and the y -axis denotes the direction of the ridgeline/drainage divide. The hillslopes incline towards a fixed surface level at $x = \pm l_x/2$, which is taken as zero for the elevation reference ($z = 0$). With sediment and water flux not crossing over the top of the divide, the boundary conditions for z and a can be written as $dz/dx = 0$ and $a = 0$ at $x = 0$. With the elevation declining monotonically on either side of the divide, the steady-state solution for specific drainage area is simply the relation $a_0 = x$ with $x \in [0, l_x/2]$. Namely, it increases linearly with the distance from the ridgeline, as shown in figure 1(b). The subscript 0 is used here to represent the base state. The steady-state solution for the smooth elevation field $z(x)$ depends on the value of exponents m and n . This solution can be obtained analytically only for $m = n = 1$, where it takes the form of a generalized hypergeometric function (Bonetti et al., 2019, 2020; Anand et al., 2020), while it has to be obtained numerically for generic exponents m and n , as discussed in Section 3. We refer to this solution as $z_0(x)$ in the stability analysis formulation.

276

2.3 Linearized Perturbed Equations

277

278

279

280

281

282

283

Having established the base-state solutions, we can now study when they become unstable to small perturbations that lead to the formation of first channels with a specific length scale. A normal-mode linear stability analysis provides a way to systematically detect the inception of this channel instability and the preferential selection of the least stable wavenumber. We refer to the following references for an extensive description of this approach and its applications in various other physical systems (Koch & Meinhardt, 1994; Drazin & Reid, 2004; Chandrasekhar, 2013; Vlade et al., 2019).

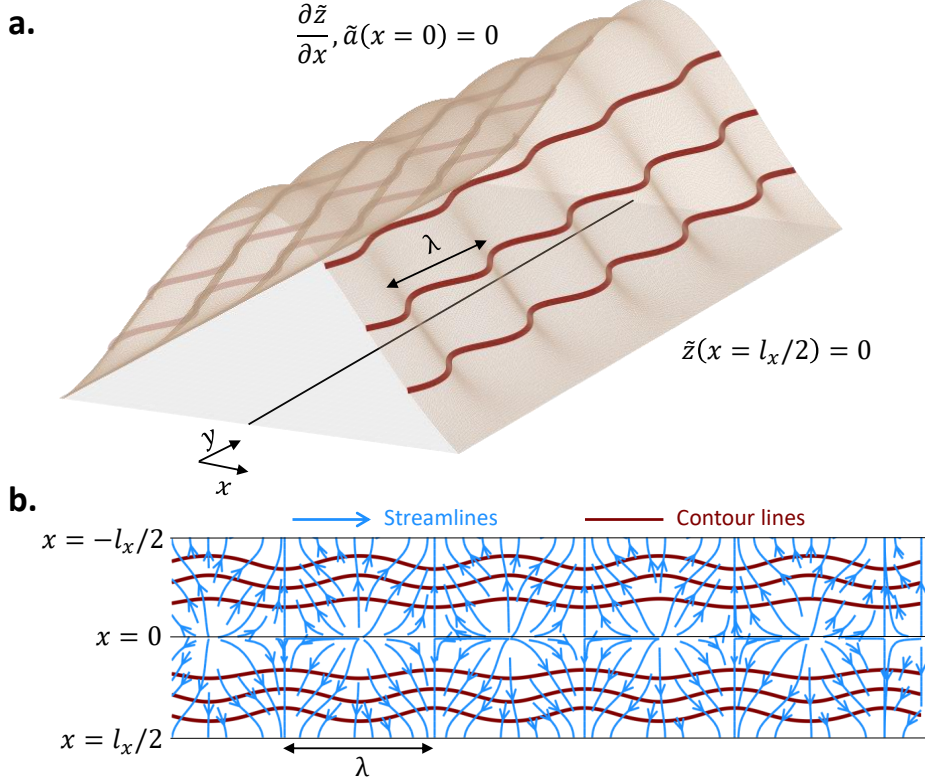


Figure 2. Schematic diagram presenting the perturbed state of the landscape used in the normal-mode analysis and the homogeneous boundary conditions. The weak perturbation \tilde{z} has been exaggerated for better visualization. (a): A representative 3D surface z is displayed, where x -axis/ y -axis denotes the direction along the hillslope/ridgeline. The perturbation with wavenumber k corresponds to the spatial wavelength $\lambda (= 2\pi/k)$. (b): The horizontal projection of the surface is shown with streamlines (in blue) perpendicular to the projected contour lines (in brown). The projected streamlines converge at the equally-spaced emerging valleys and diverge at the corresponding interlocked ridges.

284

285

286

287

288

289

With infinitesimal perturbations in the base-state solutions, the modified elevation and specific drainage area fields can be written as $z(x, y, t) = z_0(x) + \tilde{z}(x, y, t)$ and $a(x, y, t) = a_0(x) + \tilde{a}(x, y, t)$. Here $z_0(x)$ and $a_0(x)$ are the unchanneled 1D solutions discussed in Section 2.2. $\tilde{z}(x, y, t)$ and $\tilde{a}(x, y, t)$ denote the weak perturbations over the unchanneled solutions. We assume here homogeneous boundary conditions for the weak perturbations, namely $\tilde{z} = 0$ at $x = l_x/2$ and $\partial \tilde{z} / \partial x = \tilde{a} = 0$ at $x = 0$. The mathemati-

cal expressions for \tilde{z} and \tilde{a} are written as

$$\tilde{z} = \psi(x) \exp(iky + \sigma t) + \text{c.c.}, \quad (6)$$

$$\tilde{a} = \phi(x) \exp(iky + \sigma t) + \text{c.c.}, \quad (7)$$

where $\psi(x)$ and $\phi(x)$ represent perturbation amplitudes varying along the hillslope with angular wavenumber k in the y -direction and initial growth rate σ (c.c. refer to complex conjugation). Depending on σ being greater or lower than zero, the perturbation of a particular wavenumber grows or decays over time. A representation of the modified elevation field with the weak perturbation form taken in equations (6) and (7) is displayed in Figure 2.

As shown in Appendix A, substituting the above forms of perturbations for the modified z and a fields in equations (3) and (4) and linearizing, the coupled governing equations for $\psi(x)$ and $\phi(x)$ become

$$\sigma\psi = D_c \frac{d^2\psi}{dx^2} - D_c k^2 \psi - mK_e S_0^n x^{m-1} \phi + nK_e S_0^{n-1} x^m \frac{d\psi}{dx}, \quad (8)$$

$$\frac{d\phi}{dx} = -\frac{k^2 x}{S_0} \psi, \quad (9)$$

where $S_0(x) = \left| \frac{dz_0}{dx} \right|$ is the steady-state unchannelized topographic slope.

To obtain the solutions for the growth of the perturbations using the spectral technique, we recast the reference system from x to \hat{s} ($= 4x/l_x - 1$) to keep the domain between -1 and 1, so that the Legendre polynomials could be used as the basis functions in the spectral solver. By applying this reference-change and non-dimensionalizing equations (8) and (9), a differential equation in terms of $\hat{\phi}$ ($= \phi/l_x$) reads

$$\gamma_1(\hat{s}) \frac{d^3 \hat{\phi}}{d\hat{s}^3} + \gamma_2(\hat{s}) \frac{d^2 \hat{\phi}}{d\hat{s}^2} + \gamma_3(\hat{s}) \frac{d\hat{\phi}}{d\hat{s}} + \gamma_4(\hat{s}) \hat{\phi} = \hat{\sigma} \gamma_5(\hat{s}) \frac{d\hat{\phi}}{d\hat{s}}, \quad (10)$$

where the overhat ($\hat{\cdot}$) refers to the non-dimensional form of the physical quantity. The above-mentioned homogeneous boundary conditions for perturbations can be re-written as $\hat{\phi}(\hat{s} = -1) = \hat{\phi}''(\hat{s} = -1) = \hat{\phi}'(\hat{s} = 1) = 0$. We refer to Appendix B for the derivation of the above equation as well as boundary conditions in terms of $\hat{\phi}(\hat{s})$. The expressions for all coefficients are provided in table B2 (Appendix B).

Equation (10) with the imposed boundary conditions forms an eigenvalue problem, where non-zero solutions $\hat{\phi}(\hat{s})$ exist for unique (eigen)values of the growth rate $\hat{\sigma}$ ($= \sigma l_x^2 / D_c$). This system can be solved to compute the growth rate $\hat{\sigma}$ for perturbation $\hat{\phi}(\hat{s})$ of wavenumber \hat{k} at different $\mathcal{C}_{\mathcal{I}}$ values. By increasing $\mathcal{C}_{\mathcal{I}}$, a critical threshold of this dimensionless quantity, say $\mathcal{C}_{\mathcal{I}cr}$, can be found for which at least one of many possible perturbations starts growing with a positive rate $\hat{\sigma}$. By tracking the wavenumber k_{cr} with the highest positive growth rate at $\mathcal{C}_{\mathcal{I}cr}$, the spacing between emerged first-order valleys $\lambda_{cr} = 2\pi/k_{cr}$ can be computed. Hence, the required proportion of erosion and creep and the resulting valley spacing on channelization onset can be obtained by replicating this approach for different degrees of nonlinearities in m and n .

To proceed toward a solution, we converted the differential problem of equation (10) into an integral form. This is usually referred to as a weak formulation of the problem due to a reduction in the differentiability constraint of the solution. The weak formulation was then solved by utilizing a spectral technique based on the Galerkin projection with numerical quadrature (Canuto et al., 2006). We employed the algorithm proposed by Swarztrauber (2003) to compute quadrature points and weights for the numerical quadrature. To guarantee an acceptable spectral accuracy, we used 200 points between -1 and 1 for the presented results. A detailed explanation of the developed methodology and the spectral solver is provided in Appendix C.

3 The Emergence of First Channel Instability

The unchannelized slope $\hat{S}_0(\hat{s})$ as well as its first and second derivatives for different values of $\mathcal{C}_{\mathcal{I}}$ are needed to finalize the form of non-constant coefficients and solve the eigenvalue problem posed in equation (10); see table B2. These expressions are analytically attainable only for the case of unitary exponents m and n , where the unchannelized slope and its derivatives take the form of Dawson functions (see equation (12)). For any other values of m and n , these derivatives have to be obtained numerically. \hat{S}_0 ($= |d\hat{z}_0/d\hat{s}|$) can be computed by first recasting the 1D form of equation (3) in terms of \hat{S}_0 at steady-state as

$$\frac{d\hat{S}_0}{d\hat{s}} = \frac{1}{16} \left[1 - 4^{n-m} \mathcal{C}_{\mathcal{I}} (\hat{s} + 1)^m \hat{S}_0^n \right], \quad (11)$$

which then can be integrated numerically with appropriate boundary conditions for any m and n values.

We solved here the differential equation (11) with the initial value $\hat{S}_0(\hat{s} = -1) = 0$. Once the numerical solution of \hat{S}_0 was obtained, the form of \hat{S}_0' was computed by using equation (11) at the discrete quadrature points. \hat{S}_0'' was then obtained by using second-order accurate central difference of \hat{S}_0' at the interior quadrature points and first-order accurate finite difference at the boundary points.

3.1 Verification of the Numerical Solver

We performed a code verification to ensure that the developed spectral eigenvalue solver (i.e., using the numerical form of slope and its derivatives) correctly solves the stability problem, without any programming/numerical error (Roache, 1998; Oberkampf & Roy, 2010). For that, the results using numerical integration of \hat{S}_0 (and its derivatives) were compared with the linear stability results employing the analytical solution for \hat{S}_0 for the case of $m = n = 1$. The analytical expression for the slope in the case of the unitary exponents is

$$\hat{S}_0 = \mathcal{D} \left(\frac{(\hat{s} + 1)\sqrt{\mathcal{C}_{\mathcal{I}}}}{4\sqrt{2}} \right) / (2\sqrt{2\mathcal{C}_{\mathcal{I}}}), \quad (12)$$

where $\mathcal{D}(\cdot)$ is the Dawson function (Bonetti et al., 2019, 2020; Anand et al., 2020).

All the predictions from the linear stability analysis are shown for the length scale $l_x = 100$ m. Figure 3 shows the stability analysis results using numerical integration of equation (11) for the base-state. In panel a, each curve represents the growth rate for different wavenumbers of lateral perturbations at a given $\mathcal{C}_{\mathcal{I}}$. The red curve in the panel shows the critical value $\mathcal{C}_{\mathcal{I}_{cr}} \approx 37$ for which the fastest growth rate becomes positive for the intermediate wavenumber $k_{cr} \approx 0.153 \text{ m}^{-1}$. This numerical prediction of channel initiation matches with the predictions using the Dawson functions in Bonetti et al. (2020). The marginal/neutral stability curve is also shown in Figure 3b to present the transition of an unchannelized hillslope from a stable to unstable state as the critical value of the channelization index is reached. The system here displays a type I linear instability, which is similar to the Orr–Sommerfeld stability problem for the plane Poiseuille flow (Cross & Hohenberg, 1993).

3.2 The Influence of Different m Values

The values of m and n describe the coupling of the specific drainage area and local slope in the fluvial erosion mechanism. A thorough review of these power-law relationships derived from either shear stress or unit stream power law compared with the evidence from field studies is discussed in Whipple and Tucker (1999) and Lague (2014). In modeling studies of landscape evolution, the value of n is typically taken as unity with a usual range of the exponent reported between 0.67 and 1.67 (Seidl et al., 1992; Per-

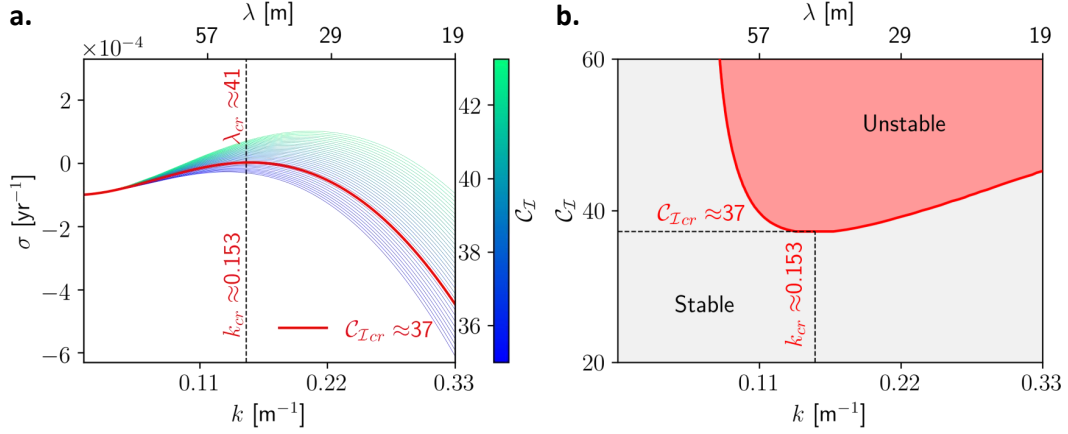


Figure 3. Linear stability analysis for the exponents $m = n = 1$ and the domain length-scale $l_x = 100$ m. (a) Growth rate σ as a function of wavenumber k for different values of C_I . The red curve corresponds to $C_I \approx 37$ with first positive growth rate for $k_{cr} \approx 0.153$ m⁻¹, which is equivalent to a characteristic incipient valley spacing $\lambda_{cr} = 2\pi/k_{cr} \approx 41$ m. (b) Marginal stability curve (the solid red curve) characterizes the instability of the base-state to the lateral perturbations. The red region designates the unstable wavenumbers with positive growth rate and the gray region describes the stable wavenumbers for distinct values of C_I .

ron et al., 2009). The value of the exponent m is usually between 0.3 and 0.8 in literature based on the analysis of the stream profiles from digital elevation models, field and map studies (Flint, 1974; Tarboton et al., 1991; Slingerland et al., 1998; Snyder et al., 2000; G. Tucker & Whipple, 2002; Bonetti et al., 2019). Exponent m equal to 0.5 is generally taken as the base case in the Optimal Channel Network (OCN) theory due to its close resemblance with scaling laws obtained in fluvial landscapes with negligible diffusive soil creep, i.e., $C_I \rightarrow \infty$ (Banavar et al., 1997; Rodriguez-Iturbe & Rinaldo, 2001; Rinaldo et al., 2014; Hooshyar et al., 2020).

We show here the role of the exponent m on the emergence of first-order valleys for $n = 1$, while the non-unity value of n is further examined in Section 3.3. Figure 4a displays the marginal stability curves obtained for eight values of m between 0.125 (red curve) and 1 (blue curve), where the corresponding horizontal lines represent the channelization threshold $C_{I,cr}$ and the vertical lines mark the fastest-growing wavenumber k_{cr} . Figure 4 b,c display the dependency of the channelization threshold and emerging valley spacing on the value of m . Specifically, as m decreases, an increase in the critical C_I value is observed together with the formation of narrower valleys at the instance of channelization.

Using the definition of the channelization index C_I given in equation (5), it can be seen that the system's behavior evolves independent of the uplift rate for $n = 1$ and is primarily governed by the ratio of the coefficient of erosion (K_e) to the soil creep (D_c) for the same length-scale of the domain. Describing the above results for channel instability in terms of $K_e/D_{c,cr}$ ($= C_{I,cr}/l_x^{m+1}$) provides insight on the efficiency level of erosion needed to initiate the channelization in natural landscapes. As displayed in the inset of panel b, the ratio of K_e to D_c grows by a factor of almost 100 for the reduction in the value of m by a factor of 8 from 1.0 to 0.125. This increase in the erosion threshold for the appearance of first-order valleys as m approaches zero reveals the importance of non-locality conveyed by a in the erosion mechanism on the development of channels in fluvial landscapes.

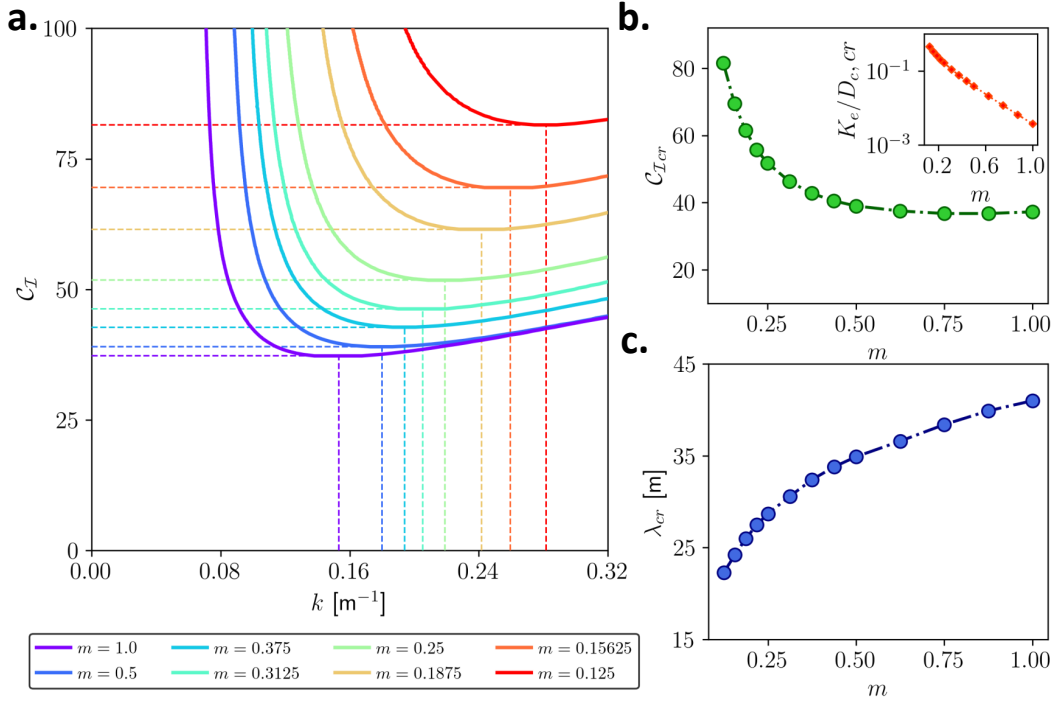


Figure 4. The effect of the drainage area exponent m on threshold of erosion intensity for the channelization and incipient valley spacing. (a): Marginal stability curves for exponent m values varying from 0.125 to 1, keeping $n = 1$. Each stability curve of a distinct color designates a particular value of m with the same-colored vertical line denoting the most unstable wavenumber, k_{cr} , and a corresponding horizontal line of the same color indicating the critical value of channelization index, C_{Icr} , for the first channelization. (b): Plot of critical channelization index C_{Icr} versus m . The inset displays the relation between K_e/D_c and m for channelization onset. (c): Variation of the incipient valley spacing at the channelization threshold λ_{cr} as a function of m .

3.3 Numerical Simulations for Generic m and n

We compared the predictions of the linear stability analysis with the instance of the first channelization by using the numerical algorithm introduced in Anand et al. (2020) for the simulations of the complete LEM. This efficient algorithm provides an order of traversing nodes in the discrete domain so that the erosion term can be computed implicitly as an upper/lower triangular matrix system with the time complexity of the algorithm varying linearly with the number of nodes in the domain. The solutions obtained using this algorithm were verified and tested carefully against analytical predictions in Anand et al. (2020).

For these numerical simulations, we considered a rectangular domain with a high aspect ratio to numerically replicate the instability onset in the linear ridge with symmetric hillslopes, as considered in the stability analysis formulation. For all the simulations, the width and length of the domain were kept equal to 100 m and 500 m, respectively, with unit grid spacing. Fixed zero elevation boundary conditions were used and the solutions were analyzed in the middle 300 m to reduce the effect of lateral sides on the channel spacing. We used two values of $n = 0.75$ and 1.0 with $m = 0.125, 0.25, 0.375, 0.5, 0.625, 0.75$, and 1.0. The value of C_I was increased for each scenario of m and n till first-order channels were observed in the domain.

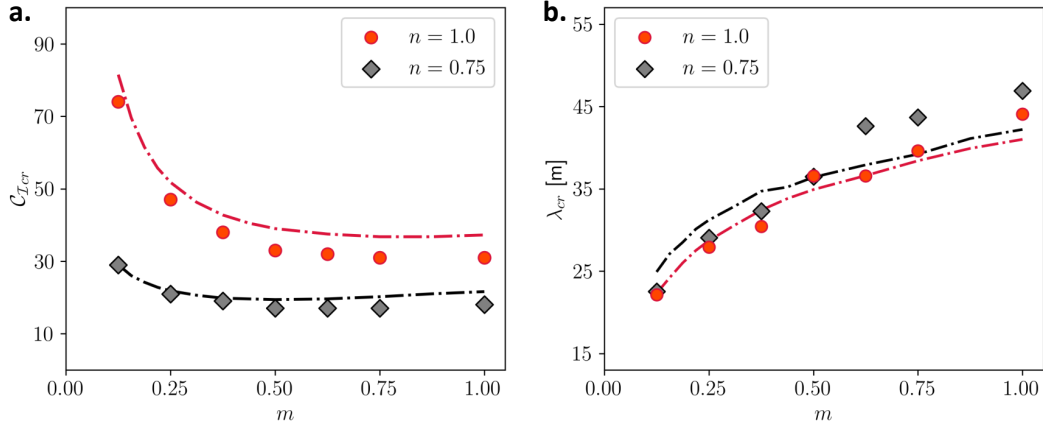


Figure 5. Comparison of predictions from linear stability analysis versus numerical simulation results in a rectangular domain (width = 100 m, length = 500 m, and 1 m grid spacing) for varying values of m with $n = 0.75$ (gray) and $n = 1.0$ (red). (a): Plot of the channelization threshold \mathcal{C}_{Icr} versus exponent m . (b): Variation of λ_{cr} as a function of m . Dashed curves represent stability analysis predictions for a given n , while symbols show results obtained from numerical simulations. A good agreement between predictions of channel initiation from the two approaches is observed across different m and n values.

Figure 5 compares the instance of the first channelization obtained using numerical simulations with results from the stability analysis. The comparison shows that the stability analysis agrees fairly well with the occurrence of first channelization and incipient valley spacing obtained in the steady-state solutions from the numerical modeling. The slight difference in \mathcal{C}_{Icr} and λ_{cr} values for the numerical model and the stability analysis hints at the nonlinear interactions (higher-order terms in the governing equations of the perturbations) discounted in the linear stability formulation that, despite being small, are present in the numerical simulations of the governing equations (3) and (4).

The channelization threshold \mathcal{C}_{Icr} increases with the lowering of the exponent m at a particular value of n . On the contrary, the value of \mathcal{C}_{Icr} grows with an increase in n at a fixed value of m . The emergent valley spacing widens for high values of m (at $n = 0.75$ and 1.0), while the exponent n has little bearing on the preferential scale of channelization at a given m . The formation of narrower valleys with the decrease in m is visible from the hillslope morphologies at the first channel instability obtained using numerical simulations (figure 6).

3.4 Comparison with Regular Valley Spacing in a Natural Landscape

We also compared the predictions from the linear stability analysis with the observations of first-order valley formation in a mountainous landscape dominated by diffusive creep and fluvial erosion. The landscape examined here is a portion of the Gabilan Mesa in California characterized by a Mediterranean climate and oak-savanna (lightly forested grassland) vegetation cover, previously investigated in Perron, Kirchner, and Dietrich (2008) and Perron et al. (2009). The displayed terrain has NE-SW trending principal channels (green) and evenly-spaced intervening hillslopes along the ridges (brown) as shown in figure 7(a,b) with the distance between the two prominent channels to be roughly 550 m and the valley spacing along the ridges around 163 ± 11 m (Perron, Kirchner, & Dietrich, 2008; Perron et al., 2009). Assuming exponent $n = 1$, the values of $D_c/K_e = 124 \pm 3$ and $m = 0.35 \pm 0.003$ were computed by using the shapes of hilltops and stream

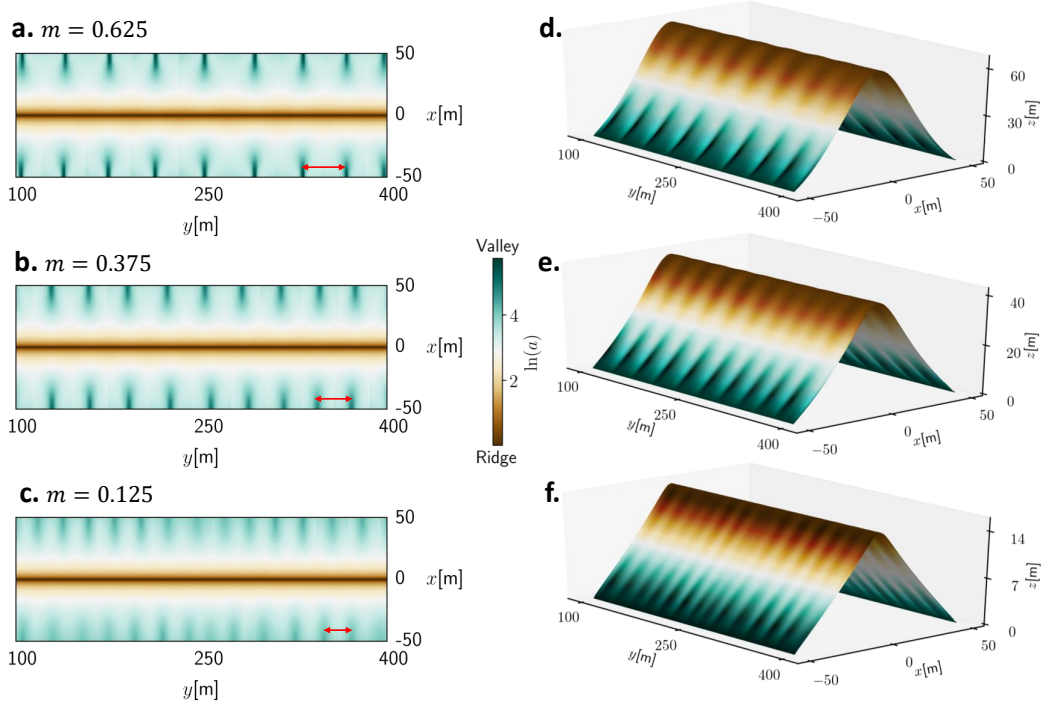


Figure 6. First channel instability observed in numerical simulations over a rectangular domain (width = 100 m, length = 500 m, and 1 m grid spacing) with $n = 1$. Plots of specific drainage area (a) field are shown for the middle 300 m (i.e., neglecting the last 100 m of the domain on both sides) for (a) $m = 0.625$ at $\mathcal{C}_{\mathcal{I}} = 32$, (b) $m = 0.375$ at $\mathcal{C}_{\mathcal{I}} = 38$, and (c) $m = 0.125$ at $\mathcal{C}_{\mathcal{I}} = 74$. The color-scale to display a field is kept the same for the presented cases to highlight the effect of an increase in the value of m with wider and larger flow accumulating in first-order valleys. Red arrows in each plot indicate typical valley spacing. (d, e, f): 3D steady-state surface profiles for the solutions shown in panels a, b, and c, respectively.

profiles for the given topography in Perron et al. (2009). Employing these values of the parameters and $l_x = 550$ m with relative uncertainties l_x and n assumed to be 2.5%, we estimated the value of $\mathcal{C}_{\mathcal{I}}$ to be 40.4 ± 7.3 .

A long ridge between two main channels resembles the domain geometry used in the stability analysis formulation. In this correspondence, fixed elevation boundary conditions at the hillslope base used in the stability analysis agree with the base level set for the Mesa landscape by the Salinas River. We conducted the linear stability analysis for $m = 0.35 \pm 0.003$ and $n = 1.0 \pm 0.025$ and tracked the instance of first channelization along with the dominant channelization mode in the calculated $\mathcal{C}_{\mathcal{I}}$ range for the landscape. The stability analysis results predict the value of $\mathcal{C}_{\mathcal{I}cr} \approx 44 \pm 3.5$, which falls in the estimated $\mathcal{C}_{\mathcal{I}}$ range for the landscape. The dominant valley spacing is computed to be 175^{+6}_{-38} m, which is also in line with the measured spacing around 163 ± 11 m in the landscape from Gabilan Mesa. Figure 7(c) shows the stability analysis result for average values of the parameters $m = 0.35$, $n = 1$, and $l_x = 550$ m.

A satisfactory agreement between the first-order valley spacing obtained from the stability analysis with those acquired by the topographic measurements of the landscape suggests that the linear stability formulation of the minimalist LEM captures well the feedback between the competing diffusive creep and fluvial erosion for the first-order chan-

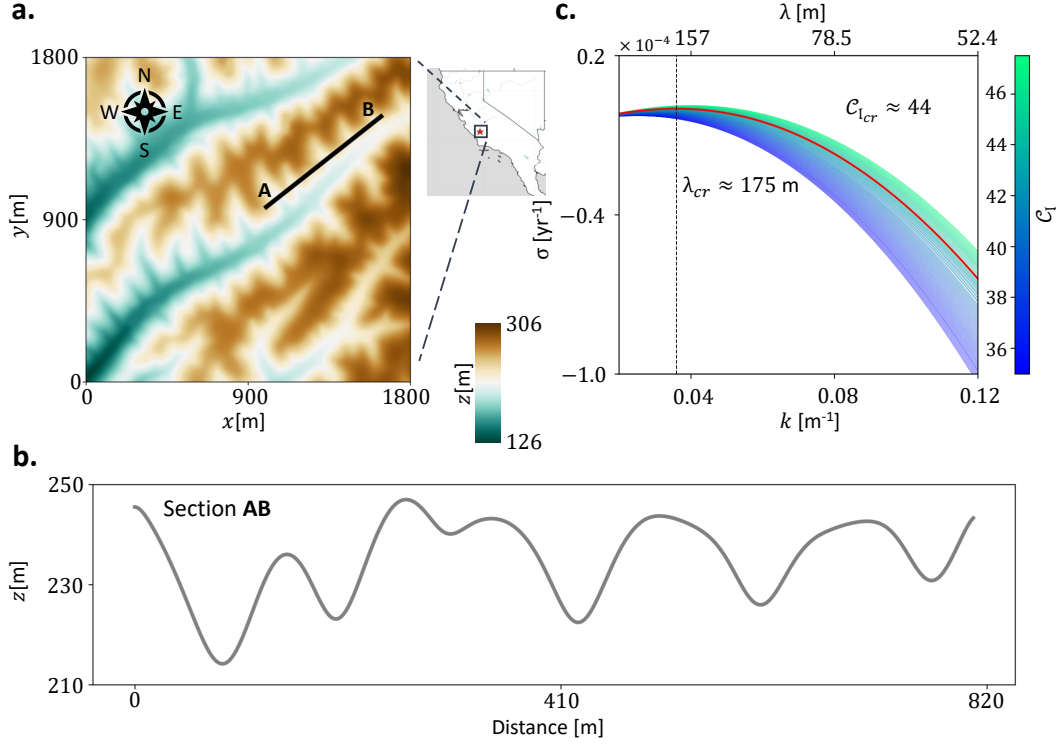


Figure 7. Comparison of the stability analysis results with the topographic data of a natural landscape. (a): 2D color-plot (top view) of the landscape covering approximately 3.25 km² area in Gabilan Mesa (California), where evenly-spaced green valleys appear along the brown mountain ridge. (b): Plot of the elevation field along the cross-section AB highlighted in panel a. The topographic data was obtained from the National Center for Airborne Laser Mapping. (c): Result of the linear stability analysis using the spectral solver for the exponents $m = 0.35$ and $n = 1$.

nelization. This is a promising result as the constant average values assumed for the parameters and the nonlinear interactions neglected in the stability analysis are approximations of the heterogeneous and noisy reality.

4 Discussion and Conclusions

We conducted a linear stability analysis of the governing equations of a minimalist DL-LEM and quantified the role of different formulations of fluvial erosion on the formation of the evenly-spaced valleys. The use of the spectral method made it feasible to compute solutions to the posed stability problem (Canuto et al., 2006; Camporeale et al., 2012), in the presence of a differential equation where non-constant coefficients elude analytical tractability. The flexibility provided by the spectral method can be extended further to quantify the effect of factors such as erosion threshold, spatially varying parameterization, etc., on the channelization in the natural landscapes.

The results have shown that the first-order valleys with spacing λ_{cr} emerge at a specific proportion of fluvial erosion and soil creep given by the critical value of the non-dimensional index $\mathcal{C}_{\mathcal{I}_{cr}}$. We obtained the dependency of λ_{cr} and $\mathcal{C}_{\mathcal{I}_{cr}}$ on the exponent m and n in the erosion mechanism. In particular, a reduction in m for a fixed value of n increases $\mathcal{C}_{\mathcal{I}_{cr}}$ threshold, which means that higher erosion potential is required to carve

the hillslope for channelization as the relative importance of the specific drainage area in the erosion mechanism diminishes. Conversely, the threshold for channel formation rises with an increase in the value of n for a particular m value. The exponent m further impacts the selection of a characteristic valley spacing with progressively narrower valleys appearing for the declining value of m .

We compared the results of the linear stability analysis with the numerical simulations of the LEM in a long rectangular domain. A close agreement between the two approaches was observed for the inception of the regularly-spaced valleys at a certain erosion threshold. Prediction of the stability analysis was further validated by using the topographic data of a natural landscape. The present analysis of the effect of the erosion law on the channelization also agrees with the observations from numerical simulations in a square domain discussed in Bonetti et al. (2020). For example, the simulated landscapes in figure 3 of Bonetti et al. (2020) show channelization and subsequent branching at higher $\mathcal{C}_{\mathcal{I}}$ values as n increases (0.7, 1.0, and 1.3) at $m = 0.5$. Similarly, the appearance of narrower primary valleys with smaller junction angles at secondary branching has been noted in the study for lower m values at a given n .

The main result of our linear stability theory is that a normal-flow hypothesis in detachment-limited conditions constitutes the minimalist water-flow model, and the counteracting diffusive creep and fluvial erosion for sediment transport create a simple system for channel formation. Numerical solutions to the posed stability problem demonstrate that preserving the spatial variability of the base-state solutions and the coefficients of the final eigenvalue problem allow a characteristic wavenumber selection based on the erosion law, providing an explicit linkage between the nonlinear erosion feedbacks and the spectral signature of channelization in the natural landscapes.

Acknowledgments

The authors acknowledge support from the US National Science Foundation (NSF) grants EAR-1331846 and EAR-1338694, Innovation Award - Moore Science-to-Action Fund, and BP through the Carbon Mitigation Initiative (CMI) at Princeton University. S.K.A. and A.P. acknowledge the support from the High Meadows Environmental Institute (HMEI). S.K.A. also acknowledges the support through the Mary and Randall Hack '69 Research Fund.

The numerical simulations in this article were performed on computational resources provided by Princeton Research Computing, a consortium of groups including the Princeton Institute for Computational Science and Engineering (PICSciE) and the Office of Information Technology's High Performance Computing Center and Visualization Laboratory at Princeton University.

Open Research

The Python code developed for the linear stability analysis is available at https://github.com/ShashankAnand1996/LEM_Stability_Analysis. Well-commented Python code for the simulation results is also accessible at <https://github.com/ShashankAnand1996/LEM>.

Appendix A Linearized Perturbed Equations and Boundary Conditions

The modified elevation and specific drainage area fields with weak perturbations can be written as

$$z(x, y, t) = z_0(x) + \tilde{z}(x, y, t), \quad (\text{A1})$$

$$a(x, y, t) = a_0(x) + \tilde{a}(x, y, t), \quad (\text{A2})$$

where $z_0(x)$ and $a_0(x)$ are the steady-state unchannelized solutions; \tilde{z} and \tilde{a} denote perturbation fields.

Using equation (A1), the updated topographic gradient vector becomes

$$\nabla z = \left(-S_0 + \frac{\partial \tilde{z}}{\partial x} \right) \mathbf{i} + \frac{\partial \tilde{z}}{\partial y} \mathbf{j}, \quad (\text{A3})$$

where $S_0(x) = \left| \frac{dz_0}{dx} \right|$ is the unchannelized local slope, \mathbf{i} is the unit vector in x -axis direction, and \mathbf{j} is the unit vector in the direction of y -axis. Employing this form of the gradient, the linearized expression for the updated topographic slope is written as

$$\begin{aligned} |\nabla z| &= \sqrt{S_0^2 + \left(\frac{\partial \tilde{z}}{\partial x} \right)^2 - 2S_0 \frac{\partial \tilde{z}}{\partial x} + \left(\frac{\partial \tilde{z}}{\partial y} \right)^2} \\ &= S_0 \left[1 + \frac{1}{2} \left(-\frac{2}{S_0} \frac{\partial \tilde{z}}{\partial x} \right) \right] = S_0 - \frac{\partial \tilde{z}}{\partial x}. \end{aligned} \quad (\text{A4})$$

The governing equation for the updated elevation field $z(x, y, t)$ is

$$\begin{aligned} \frac{\partial z}{\partial t} &= D_c \nabla^2 z - K_e a^m |\nabla z|^n + U, \\ \frac{\partial \tilde{z}}{\partial t} &= D_c \nabla^2 z_0 + D_c \nabla^2 \tilde{z} - K_e (a_0 + \tilde{a})^m \left(S_0 - \frac{\partial \tilde{z}}{\partial x} \right)^n + U, \end{aligned} \quad (\text{A5})$$

where $(a_0 + \tilde{a})^m = a_0^m + m a_0^{m-1} \tilde{a}$ for small perturbation \tilde{a} . Writing $\left(S_0 - \frac{\partial \tilde{z}}{\partial x} \right)^n = S_0^n \left(1 - \frac{1}{S_0} \frac{\partial \tilde{z}}{\partial x} \right)^n$ and performing series expansion for small $\frac{\partial \tilde{z}}{\partial x}$ modifies the term as $S_0^n - n S_0^{n-1} \frac{\partial \tilde{z}}{\partial x}$. Using these expressions and $a_0 = x$, the linearized equation for $\tilde{z}(x, y, t)$ reads

$$\frac{\partial \tilde{z}}{\partial t} = D_c \nabla^2 \tilde{z} - m K_e S_0^n x^{m-1} \tilde{a} + n K_e x^m S_0^{n-1} \frac{\partial \tilde{z}}{\partial x}. \quad (\text{A6})$$

Using equations (A3) and (A4), the unit vector in the direction of steepest descent of the updated elevation field is

$$\begin{aligned} \mathbf{n} &= -\frac{\nabla z}{|\nabla z|} = -\frac{\left(-S_0 + \frac{\partial \tilde{z}}{\partial x} \right)}{\left(S_0 - \frac{\partial \tilde{z}}{\partial x} \right)} \mathbf{i} - \frac{\frac{\partial \tilde{z}}{\partial y}}{\left(S_0 - \frac{\partial \tilde{z}}{\partial x} \right)} \mathbf{j} = \mathbf{i} - \left(\frac{S_0 - \frac{\partial \tilde{z}}{\partial x}}{\frac{\partial \tilde{z}}{\partial y}} \right)^{-1} \mathbf{j} \\ &= \mathbf{i} - \left(\frac{S_0}{\frac{\partial \tilde{z}}{\partial y}} - \frac{\frac{\partial \tilde{z}}{\partial x}}{\frac{\partial \tilde{z}}{\partial y}} \right)^{-1} \mathbf{j} = \mathbf{i} - \frac{\frac{\partial \tilde{z}}{\partial y}}{S_0} \mathbf{j}. \end{aligned} \quad (\text{A7})$$

The linearized governing equation for $\tilde{a}(x, y, t)$ can be obtained using equation (A7) as

$$\begin{aligned} \nabla \cdot (a\mathbf{n}) &= 1 \\ \nabla \cdot \left((a_0 + \tilde{a})\mathbf{i} - \frac{1}{S_0} \frac{\partial \tilde{z}}{\partial y} (a_0 + \tilde{a})\mathbf{j} \right) &= 1 \\ \frac{\partial (x + \tilde{a})}{\partial x} - \frac{1}{S_0} \frac{\partial \tilde{z}}{\partial y} \frac{\partial (x + \tilde{a})}{\partial y} - \frac{1}{S_0} \frac{\partial^2 \tilde{z}}{\partial y^2} (x + \tilde{a}) &= 1 \\ \frac{\partial \tilde{a}}{\partial x} - \frac{1}{S_0} \frac{\partial \tilde{z}}{\partial y} \frac{\partial \tilde{a}}{\partial y} - \frac{x}{S_0} \frac{\partial^2 \tilde{z}}{\partial y^2} - \frac{\tilde{a}}{S_0} \frac{\partial^2 \tilde{z}}{\partial y^2} &= 0 \\ \frac{\partial \tilde{a}}{\partial x} = \frac{x}{S_0} \frac{\partial^2 \tilde{z}}{\partial y^2} + h.o.t. = \frac{x}{S_0} \frac{\partial^2 \tilde{z}}{\partial y^2}. \end{aligned} \quad (\text{A8})$$

We employ the mathematical expressions for $\tilde{z}(x, y, t)$ and $\tilde{a}(x, y, t)$ as

$$\tilde{z} = \psi(x) \exp(iky + \sigma t) + \text{c.c.}, \quad (\text{A9})$$

$$\tilde{a} = \phi(x) \exp(iky + \sigma t) + \text{c.c.}, \quad (\text{A10})$$

where $\psi(x)$ and $\phi(x)$ denote perturbation amplitudes varying along the hillslope with angular wavenumber k in the y -direction and initial growth rate σ . Substituting these in equations (A6) and (A8), we write the coupled equations for $\psi(x)$ and $\phi(x)$ as

$$\sigma\psi = D_c \frac{d^2\psi}{dx^2} - D_c k^2 \psi - mK_e S_0^n x^{m-1} \phi + nK_e S_0^{n-1} x^m \frac{d\psi}{dx}, \quad (\text{A11})$$

$$\frac{d\phi}{dx} = -\frac{k^2 x}{S_0} \psi. \quad (\text{A12})$$

In this work, we assume homogeneous boundary conditions for the weak perturbations, namely $\tilde{a} = 0$ at $x = 0$, $\tilde{z} = 0$ at $x = l_x/2$, and $\partial\tilde{z}/\partial x = 0$ at $x = 0$. These three conditions are re-written in terms of only $\phi(x)$ to proceed towards a solution, as shown below.

Using equation (A10), $\tilde{a} = 0$ at $x = 0$ becomes $\phi(x = 0) = 0$. The condition $\tilde{z} = 0$ at $x = l_x/2$ gives $\psi(x = l_x/2) = 0$ by using equation (A9). Substituting this relation in equation (A12) provides $d\phi/dx(x = l_x/2) = 0$. Finally, $\frac{\partial\tilde{z}}{\partial x} = 0$ at $x = 0$ gets translated into $\frac{d\psi}{dx} = 0$ at $x = 0$. Imposing this requirement in equation (A12) gives $\frac{d}{dx} \left(\frac{S_0}{x} \frac{d\phi}{dx} \right) \Big|_{x=0} = 0$. Under the assumption that $S_0(x)$ behaves linearly in the limit $x \rightarrow 0$, we get the boundary condition $\frac{d^2\phi}{dx^2}(x = 0) = 0$.

Appendix B Non-dimensionalization and Eigenvalue Problem Formulation

The physical problem posed here has three primary dimensions, namely vertical direction (Z) for the elevation field, horizontal direction (X) for spatial extent of the solution domain, and time (T) for the rate of evolution. Using l_x as the horizontal scale, $\frac{Ul_x^2}{D_c}$ as the vertical scale, and $\frac{l_x^2}{D_c}$ as the time scale, perturbed equations (A11) and (A12) can be recast in the following dimensionless form

$$\hat{\sigma}\hat{\psi} = -\hat{k}^2\hat{\psi} + \frac{d^2\hat{\psi}}{d\hat{x}^2} - m\mathcal{C}_{\mathcal{I}}\hat{S}_0^n\hat{x}^{m-1}\hat{\phi} + n\mathcal{C}_{\mathcal{I}}\hat{S}_0^{n-1}\hat{x}^m\frac{d\hat{\psi}}{d\hat{x}}, \quad (\text{B1})$$

$$\frac{d\hat{\phi}}{d\hat{x}} = -\frac{\hat{k}^2\hat{x}}{\hat{S}_0}\hat{\psi}, \quad (\text{B2})$$

$$\mathcal{C}_{\mathcal{I}} = \frac{K_e l_x^{m+n}}{D_c^n U^{1-n}}, \quad (\text{B3})$$

where the overhat notation ($\hat{\cdot}$) refers to the non-dimensional form of the physical quantities. The channelization index $\mathcal{C}_{\mathcal{I}}$ is the non-dimensional quantity that represents the tendency of the system to form channels. Table B1 presents the non-dimensionalized forms of the variables involved in the above equations.

Table B1. Variables present in the perturbed equations (A11) and (A12) along with their dimension functions and non-dimensionalized forms used in equations (B1) and (B2).

| Variable | Dimension Function | Non-dimensionalized Form |
|----------|--------------------|--|
| σ | T^{-1} | $\hat{\sigma} = \sigma \frac{l_x^2}{D}$ |
| ψ | Z | $\hat{\psi} = \psi \frac{\hat{D}_c}{Ul_x^2}$ |
| ϕ | L | $\hat{\phi} = \frac{\phi}{l_x}$ |
| k | L^{-1} | $\hat{k} = kl_x$ |
| S_0 | ZL^{-1} | $\hat{S}_0 = S_0 \frac{D_c}{Ul_x}$ |
| x | L | $\hat{x} = \frac{x}{l_x}$ |

Combining equations (B1) and (B2) and changing the reference variable from \hat{x} to \hat{s} ($= 4\hat{x} - 1$), the final form of the perturbed equation in terms of only $\hat{\phi}(\hat{s})$ reads

$$\gamma_1(\hat{s})\hat{\phi}''' + \gamma_2(\hat{s})\hat{\phi}'' + \gamma_3(\hat{s})\hat{\phi}' + \gamma_4(\hat{s})\hat{\phi} = \hat{\sigma}\gamma_5(\hat{s})\hat{\phi}', \quad (\text{B4})$$

where the prime ($'$) refers to the derivative with respect to \hat{s} . The expressions for coefficients are specified in table B2.

Table B2. Constants and expressions for the coefficients in the differential eigenvalue problem (equation (10) in the main text). The prime ($'$) refers to the derivative with respect to \hat{s} .

| Name | Form of the constant/expression |
|----------------------|--|
| a_1 | $\frac{n\mathcal{C}_{\mathcal{I}}}{4^{m-n}}$ |
| a_2 | \hat{k}^2 |
| a_3 | $\frac{m\mathcal{C}_{\mathcal{I}}\hat{k}^2}{4^{2+m-n}}$ |
| $\hat{S}_0(\hat{s})$ | $ d\hat{z}_0/d\hat{s} $ |
| $\gamma_1(\hat{s})$ | $16\hat{S}_0^2(\hat{s}+1)^2$ |
| $\gamma_2(\hat{s})$ | $-32\hat{S}_0^2(\hat{s}+1) + 32\hat{S}_0\hat{S}_0'(\hat{s}+1)^2 + a_1\hat{S}_0^{n+1}(\hat{s}+1)^{m+2}$ |
| $\gamma_3(\hat{s})$ | $16\hat{S}_0\hat{S}_0''(\hat{s}+1)^2 - 32\hat{S}_0\hat{S}_0'(\hat{s}+1) + 32\hat{S}_0^2 - a_2\hat{S}_0^2(\hat{s}+1)^2 - a_1\hat{S}_0^{n+1}(\hat{s}+1)^{m+1} + a_1\hat{S}_0^n\hat{S}_0'(\hat{s}+1)^{m+2}$ |
| $\gamma_4(\hat{s})$ | $a_3\hat{S}_0^{n+1}(\hat{s}+1)^{m+2}$ |
| $\gamma_5(\hat{s})$ | $\hat{S}_0^2(\hat{s}+1)^2$ |

Finally, the boundary conditions for $\hat{\phi}(\hat{s})$ in the changed reference variable \hat{s} are

$$\hat{\phi} = 0 \quad (\hat{s} = -1), \quad (\text{B5})$$

$$\hat{\phi}' = 0 \quad (\hat{s} = 1), \quad (\text{B6})$$

$$\hat{\phi}'' = 0 \quad (\hat{s} = -1). \quad (\text{B7})$$

Appendix C Weak Formulation and Galerkin Discretization

Equation (B4) along with boundary conditions mentioned in equations (B5), (B6), and (B7) constitute an eigenvalue problem, which is solved here by transforming the final equation into an integral form (weak formulation). The dependency on \hat{s} has been omitted hereafter in the expressions for the ease of notation.

A weak formulation is obtained by multiplying both sides of equation (B4) by a generic L^2 -test function v_i (with $i \in 1, N$) and integrating over the interval $(-1, 1)$ as

$$\left(\gamma_1 \hat{\phi}''', v_i\right) + \left(\gamma_2 \hat{\phi}'', v_i\right) + \left(\gamma_3 \hat{\phi}', v_i\right) + \left(\gamma_4 \hat{\phi}, v_i\right) = \hat{\sigma} \left(\gamma_5 \hat{\phi}', v_i\right), \quad (C1)$$

where $(f, g) := \int_{-1}^1 f(\hat{s}')g(\hat{s}')d\hat{s}'$ defines the inner product between two functions. The numerical approximation of inner products in the above equation can be computed by interpolatory Legendre-Gauss quadrature formula, which approximates the integration of a generic function f in the domain $[-1, 1]$ through the use of weights w_k computed at discrete (Gauss-Lobatto) nodes \hat{s}_k as

$$\int_{-1}^1 f(\hat{s})d\hat{s} \approx \sum_{k=0}^{k=K} f(\hat{s}_k)w_k. \quad (C2)$$

In the numerical solver developed for this work, \hat{s}_k and w_k are computed using the algorithm provided by Swarztrauber (2003).

Based on previous works on spectral solutions of eigenvalue problems in shear flows (Shen, 1994), we seek a solution of $\hat{\phi}$ in the form

$$\hat{\phi} = u_{-1}(\hat{s})\alpha_{-1} + u_0(\hat{s})\alpha_0 + \sum_{j=1}^N u_j(\hat{s})\alpha_j = \sum_{j=-1}^N u_j(\hat{s})\alpha_j, \quad (C3)$$

where α_j are the unknown coefficients of the linear expansion and u_j reads

$$u_{-1}(\hat{s}) = \frac{1 + \hat{s}}{2} \quad (C4)$$

$$u_0(\hat{s}) = -\frac{\hat{s}^2}{4} + \frac{\hat{s}}{2} + \frac{3}{4} \quad (C5)$$

$$u_j(\hat{s}) = \frac{L_{j+2}(\hat{s}) - L_j(\hat{s})}{\sqrt{2(2j+3)}} \quad (j \in [1, N]). \quad (C6)$$

In the above expressions, L_j represents the Legendre polynomial of degree j . So, $u_j(\pm 1) = 0$ for $j \geq 1$ with $u_{-1}(-1) = u_0(-1) = 0$. The additional functions u_{-1} and u_0 have been added to the basis to accommodate the non-vanishing boundary conditions.

Finally, from equation (C6) and using the properties of the Legendre polynomial (Szegő, 1939; Pólya & Szegő, 1972), one obtains

$$u'_j(\hat{s}) = \sqrt{\frac{2j+3}{2}} L_{j+1}(\hat{s}). \quad (C7)$$

Taking these particular forms of trial functions, the boundary condition $\phi(-1) = 0$ gets implicitly imposed in the formulation. The remaining two boundary conditions (equations (B6) and (B7)) have to be applied explicitly in the strong form, as described later. Test functions (v_i for $i \in [1, N]$) are chosen by integrating twice each Legendre poly-

nomial as

$$v_i = \sqrt{i + \frac{3}{2}} \left(\frac{L_{i+3} - L_{i+1}}{(2i+3)(2i+5)} - \frac{L_{i+1} - L_{i-1}}{(2i+1)(2i+3)} \right), \quad (\text{C8})$$

$$v'_i = \frac{L_{i+2} - L_i}{\sqrt{2(2i+3)}}, \quad (\text{C9})$$

$$v''_i = \sqrt{\frac{2i+3}{2}} L_{i+1}, \quad (\text{C10})$$

where these functions satisfy homogeneous boundary conditions as $v_i(\pm 1) = v'_i(\pm 1) = 0$.

Using integration by parts, the third-order term in equation (C1) can be written as

$$\begin{aligned} (\hat{\phi}''' \gamma_1, v_i) &= \hat{\phi}''(1) \gamma_1(1) v_i(1) - \hat{\phi}''(-1) \gamma_1(-1) v_i(-1) \\ &\quad - \hat{\phi}'(1) [\gamma'_1(1) v_i(1) + \gamma_1(1) v'_i(1)] + \hat{\phi}'(-1) [\gamma'_1(-1) v_i(-1) + \gamma_1(-1) v'_i(-1)] \\ &\quad + (\hat{\phi}', \gamma'_1 v_i + \gamma_1 v'_i) + (\hat{\phi}', \gamma'_1 v'_i + \gamma_1 v''_i). \end{aligned} \quad (\text{C11})$$

The above expression gets simplified using $v_i(\pm 1) = 0$ and $v'_i(\pm 1) = 0$ as

$$(\hat{\phi}''' \gamma_1, v_i) = (\hat{\phi}', \gamma'_1 v_i + \gamma_1 v'_i) + (\hat{\phi}', \gamma'_1 v'_i + \gamma_1 v''_i). \quad (\text{C12})$$

Similarly, the second-order term in equation (C1) is simplified to

$$(\hat{\phi}'' \gamma_2, v_i) = -(\hat{\phi}', \gamma'_2 v_i + \gamma_2 v'_i). \quad (\text{C13})$$

Using equations (C12) and (C13) and the property of symmetry for the inner product $((f, g) = (g, f))$, the weak formulation becomes

$$(\gamma'_1 v_i + 2\gamma'_1 v'_i + \gamma_1 v''_i - \gamma'_2 v_i - \gamma_2 v'_i + \gamma_3 v_i, \hat{\phi}') + (\gamma_4 v_i, \hat{\phi}) = \hat{\sigma} (\gamma_5 v_i, \hat{\phi}). \quad (\text{C14})$$

The final form of the weak formulation in terms of trial (u_j) and test functions (v_i) is obtained as

$$\sum_{j=-1, N} (\gamma'_1 v_i + 2\gamma'_1 v'_i + \gamma_1 v''_i - \gamma'_2 v_i - \gamma_2 v'_i + \gamma_3 v_i, u'_j) \alpha_j + (\gamma_4 v_i, u_j) \alpha_j = \sum_{j=-1}^{j=N} \hat{\sigma} (\gamma_5 v_i, u'_j) \alpha_j, \quad (\text{C15})$$

for $i = 1, N$. The system shown by equation (C15) consists of N equations with $N + 2$ unknowns $(\alpha_j, j \in [-1, N])$. This can also be represented in matrix notation as $\mathbf{A}\boldsymbol{\alpha} = \hat{\sigma}\mathbf{B}\boldsymbol{\alpha}$, where the matrix entries can be written as

$$\begin{aligned} A_{ij} &= \sum_{k=0}^K \left[\left((\gamma''_1(\hat{s}_k) v_i(\hat{s}_k) + 2\gamma'_1(\hat{s}_k) v'_i(\hat{s}_k) + \gamma_1(\hat{s}_k) v''_i(\hat{s}_k) - \gamma'_2(\hat{s}_k) v_i(\hat{s}_k) \right. \right. \\ &\quad \left. \left. - \gamma_2(\hat{s}_k) v'_i(\hat{s}_k) + \gamma_3(\hat{s}_k) v_i(\hat{s}_k) \right) u'_j(\hat{s}_k) + \gamma_4(\hat{s}_k) v_i(\hat{s}_k) u_j(\hat{s}_k) \right] w_k, \end{aligned} \quad (\text{C16})$$

$$B_{ij} = \sum_{k=0}^K (\gamma_5(\hat{s}_k) v_i(\hat{s}_k) u'_j(\hat{s}_k) w_k). \quad (\text{C17})$$

The next two equations are obtained by imposing boundary conditions $\phi''(-1) = 0$ and $\phi'(1) = 0$ in the strong form. Using the trial functions (and $u'_0(1) = u''_{-1}(-1) = 0$), we can write

$$u''_0(-1) \alpha_0 + u''_1(-1) \alpha_1 + u''_2(-1) \alpha_2 + \dots = 0, \quad (\text{C18})$$

$$u'_{-1}(1) \alpha_{-1} + u'_1(1) \alpha_1 + u'_2(1) \alpha_2 + \dots = 0. \quad (\text{C19})$$

The relationship between the coefficients for the imposed boundary conditions can be obtained as

$$\alpha_0 = -\frac{u_1''(-1)}{u_0''(-1)}\alpha_1 - \frac{u_2''(-1)}{u_0''(-1)}\alpha_2 - \dots = p_1\alpha_1 + p_2\alpha_2 + \dots \quad (\text{C20})$$

$$\alpha_{-1} = -\frac{u_1'(1)}{u_{-1}'(1)}\alpha_1 - \frac{u_2'(1)}{u_{-1}'(1)}\alpha_2 - \dots = q_1\alpha_1 + q_2\alpha_2 + \dots \quad (\text{C21})$$

with $p_j = -\frac{u_j''(-1)}{u_0''(-1)} = -\frac{u_j''(-1)}{-1/2}$ and $q_j = -\frac{u_j'(1)}{u_{-1}'(1)} = -\frac{u_j'(1)}{1/2}$ for $j = 1, N$.

Applying this relation among the coefficients, the modified left-hand and right-hand matrix entries read

$$A'_{i,j} = A_{i,0}p_j + A_{i,-1}q_j + A_{i,j}, \quad B'_{i,j} = B_{i,0}p_j + B_{i,-1}q_j + B_{i,j}, \quad (i, j \in [1, N]). \quad (\text{C22})$$

The algebraic system, $\mathbf{A}'\boldsymbol{\alpha} = \hat{\sigma}\mathbf{B}'\boldsymbol{\alpha}$, now consists of N equations in N unknowns ($\alpha_j, j \in [1, N]$), which can be solved as a generalized eigenvalue problem to compute the growth rate ($\hat{\sigma}$) for different values of \hat{k} and $\mathcal{C}_{\mathcal{I}}$.

References

- Ahnert, F. (1987). Approaches to dynamic equilibrium in theoretical simulations of slope development. *Earth Surface Processes and Landforms*, 12(1), 3–15.
- Allen, P. (2005). Striking a chord. *Nature*, 434(7036), 961–961.
- Anand, S. K., Hooshyar, M., & Porporato, A. (2020). Linear layout of multiple flow-direction networks for landscape-evolution simulations. *Environmental Modelling & Software*, 133, 104804.
- Attal, M., Tucker, G., Whittaker, A. C., Cowie, P., & Roberts, G. P. (2008). Modeling fluvial incision and transient landscape evolution: Influence of dynamic channel adjustment. *Journal of Geophysical Research: Earth Surface*, 113(F3).
- Banavar, J. R., Colaiori, F., Flammini, A., Giacometti, A., Maritan, A., & Rinaldo, A. (1997). Sculpting of a fractal river basin. *Physical review letters*, 78(23), 4522.
- Birnir, B., Smith, T. R., & Merchant, G. E. (2001). The scaling of fluvial landscapes. *Computers & geosciences*, 27(10), 1189–1216. doi: 10.1016/S0098-3004(01)00022-X
- Bonetti, S., Bragg, A., & Porporato, A. (2018). On the theory of drainage area for regular and non-regular points. *Proceedings of the Royal Society A: Mathematical, Physical and Engineering Sciences*, 474(2211), 20170693.
- Bonetti, S., Hooshyar, M., Camporeale, C., & Porporato, A. (2020). Channelization cascade in landscape evolution. *Proceedings of the National Academy of Sciences*. doi: 10.1073/pnas.1911817117
- Bonetti, S., Richter, D. D., & Porporato, A. (2019). The effect of accelerated soil erosion on hillslope morphology. *Earth Surface Processes and Landforms*, 44(15), 3007–3019.
- Camporeale, C. (2015). Hydrodynamically locked morphogenesis in karst and ice flutings. *Journal of Fluid Mechanics*, 778, 89–119.
- Camporeale, C., Canuto, C., & Ridolfi, L. (2012). A spectral approach for the stability analysis of turbulent open-channel flows over granular beds. *Theoretical and Computational Fluid Dynamics*, 26(1-4), 51–80.
- Camporeale, C., & Ridolfi, L. (2012). Ice ripple formation at large reynolds numbers. *Journal of fluid mechanics*, 694, 225–251.
- Canuto, C. G., Hussaini, M. Y., Quarteroni, A., & Zang, T. A. (2006). *Spectral methods: Fundamentals in single domains*. Berlin: Springer.

- Carson, M., & Kirkby, M. (1972). *Hillslope form and process, by m.a. carson and m.j. kirkby*. Retrieved from <https://books.google.com/books?id=LuKKWgEACAAJ>
- Chandrasekhar, S. (2013). *Hydrodynamic and hydromagnetic stability*. Courier Corporation.
- Chen, A., Darbon, J., & Morel, J.-M. (2014). Landscape evolution models: A review of their fundamental equations. *Geomorphology*, 219, 68–86. doi: 10.1016/j.geomorph.2014.04.037
- Collins, D. B. G., Bras, R. L., & Tucker, G. E. (2004). Modeling the effects of vegetation-erosion coupling on landscape evolution. *Journal of Geophysical Research: Earth Surface*, 109(F3).
- Coulthard, T. J., Neal, J. C., Bates, P. D., Ramirez, J., de Almeida, G. A., & Hancock, G. R. (2013). Integrating the lisflood-fp 2d hydrodynamic model with the caesar model: implications for modelling landscape evolution. *Earth Surface Processes and Landforms*, 38(15), 1897–1906.
- Cross, M. C., & Hohenberg, P. C. (1993). Pattern formation outside of equilibrium. *Reviews of modern physics*, 65(3), 851.
- Culling, W. E. H. (1963). Soil creep and the development of hillside slopes. *The Journal of Geology*, 71(2), 127–161.
- Davy, P., & Lague, D. (2009). Fluvial erosion/transport equation of landscape evolution models revisited. *Journal of Geophysical Research: Earth Surface*, 114(F3).
- Drazin, P. G., & Reid, W. H. (2004). *Hydrodynamic stability*. Cambridge university press.
- Flint, J.-J. (1974). Stream gradient as a function of order, magnitude, and discharge. *Water Resources Research*, 10(5), 969–973.
- Fowler, A. (2011). *Mathematical geoscience* (Vol. 36). Springer Science & Business Media. doi: 10.1007/978-0-85729-721-1
- Gabet, E. J., Reichman, O., & Seabloom, E. W. (2003). The effects of bioturbation on soil processes and sediment transport. *Annual Review of Earth and Planetary Sciences*, 31(1), 249–273.
- Gallant, J. C., & Hutchinson, M. F. (2011). A differential equation for specific catchment area. *Water Resources Research*, 47(5). doi: 10.1029/2009WR008540
- Gilbert, C. G., & Dutton, C. E. (1880). *Report on the geology of the henry mountains*. US Government Printing Office.
- Hallet, B. (1990). Spatial self-organization in geomorphology: from periodic bedforms and patterned ground to scale-invariant topography. *Earth-Science Reviews*, 29(1-4), 57–75.
- Hancock, G., Lowry, J., Coulthard, T., Evans, K., & Moliere, D. (2010). A catchment scale evaluation of the siberia and caesar landscape evolution models. *Earth Surface Processes and Landforms*, 35(8), 863–875.
- Hergarten, S. (2020). Transport-limited fluvial erosion—simple formulation and efficient numerical treatment. *Earth Surface Dynamics*, 8(4), 841–854.
- Hooshyar, M., Anand, S., & Porporato, A. (2020). Variational analysis of landscape elevation and drainage networks. *Proceedings of the Royal Society A*, 476(2239), 20190775.
- Hooshyar, M., Katul, G., & Porporato, A. (2021). Spectral signature of landscape channelization. *Geophysical Research Letters*, 48(8), e2020GL091015.
- Howard, A. D. (1994). A detachment-limited model of drainage basin evolution. *Water Resources Research*, 30(7), 2261–2285.
- Izumi, N., & Parker, G. (1995). Inception of channelization and drainage basin formation: upstream-driven theory. *Journal of Fluid Mechanics*, 283, 341–363.
- Izumi, N., & Parker, G. (2000). Linear stability analysis of channel inception: downstream-driven theory. *Journal of Fluid Mechanics*, 419, 239–262.

- Kirkby, M. (1971). Hillslope process-response models based on the continuity equation. *Inst. Br. Geogr. Spec. Publ*, 3(1), 5–30.
- Koch, A., & Meinhardt, H. (1994). Biological pattern formation: from basic mechanisms to complex structures. *Reviews of modern physics*, 66(4), 1481.
- Lague, D. (2014). The stream power river incision model: evidence, theory and beyond. *Earth Surface Processes and Landforms*, 39(1), 38–61.
- Leopold, L. B., & Maddock, T. (1953). *The hydraulic geometry of stream channels and some physiographic implications* (Vol. 252). US Government Printing Office.
- Loewenherz, D. S. (1991). Stability and the initiation of channelized surface drainage: a reassessment of the short wavelength limit. *Journal of Geophysical Research: Solid Earth*, 96(B5), 8453–8464.
- Loewenherz-Lawrence, D. (1994). Hydrodynamic description for advective sediment transport processes and rill initiation. *Water Resources Research*, 30(11), 3203–3212.
- Oberkampf, W. L., & Roy, C. J. (2010). *Verification and validation in scientific computing*. Cambridge University Press. doi: 10.1017/cbo9780511760396.001
- Parker, G., & Izumi, N. (2000). Purely erosional cyclic and solitary steps created by flow over a cohesive bed. *Journal of Fluid Mechanics*, 419, 203–238.
- Pelletier, J. D. (2012). Fluvial and slope-wash erosion of soil-mantled landscapes: detachment-or transport-limited? *Earth Surface Processes and Landforms*, 37(1), 37–51.
- Perron, J. T., Dietrich, W. E., & Kirchner, J. W. (2008). Controls on the spacing of first-order valleys. *Journal of Geophysical Research: Earth Surface*, 113(F4).
- Perron, J. T., Kirchner, J. W., & Dietrich, W. E. (2008). Spectral signatures of characteristic spatial scales and nonfractal structure in landscapes. *Journal of Geophysical Research: Earth Surface*, 113(F4).
- Perron, J. T., Kirchner, J. W., & Dietrich, W. E. (2009). Formation of evenly spaced ridges and valleys. *Nature*, 460, 502–505.
- Pólya, G., & Szegő, G. (1972). *Problems and theorems in analysis: Series, integral calculus, theory of functions*. Springer.
- Porporato, A. (2022). Hydrology without dimensions. *Hydrology and Earth System Sciences*, 26(2), 355–374.
- Rinaldo, A., Rigon, R., Banavar, J. R., Maritan, A., & Rodriguez-Iturbe, I. (2014). Evolution and selection of river networks: Statics, dynamics, and complexity. *Proceedings of the National Academy of Sciences*, 111(7), 2417–2424.
- Roache, P. J. (1998). *Verification and validation in computational science and engineering*. Hermosa.
- Rodriguez-Iturbe, I., & Rinaldo, A. (2001). *Fractal river basins: chance and self-organization*. Cambridge University Press.
- Roering, J. J. (2008). How well can hillslope evolution models “explain” topography? simulating soil transport and production with high-resolution topographic data. *Geological Society of America Bulletin*, 120(9-10), 1248–1262. doi: 10.1130/B26283.1
- Seidl, M., Dietrich, W., Schmidt, K., & de Ploey, J. (1992). The problem of channel erosion into bedrock. *Functional geomorphology*, 101–124.
- Shaler, N. (1899). Spacing of rivers with reference to hypothesis of baseleveling. *Bulletin of the Geological Society of America*, 10(1), 263–276.
- Shen, J. (1994). Efficient spectral-Galerkin methods I. direct solvers for the second and fourth order equations using Legendre polynomials. *SIAM Journal on Scientific Computing*, 15(6), 1489–1505.
- Singh, A., Reinhardt, L., & Foufoula-Georgiou, E. (2015). Landscape reorganization under changing climatic forcing: Results from an experimental landscape. *Water Resources Research*, 51(6), 4320–4337.

- Slingerland, R., Willett, S., & Hovius, N. (1998). Slope-area scaling as a test of fluvial bedrock erosion laws. *Eos Trans. AGU*, 79(45).
- Smith, T. R. (2010). A theory for the emergence of channelized drainage. *Journal of Geophysical Research: Earth Surface*, 115(F2).
- Smith, T. R., & Bretherton, F. P. (1972). Stability and the conservation of mass in drainage basin evolution. *Water Resources Research*, 8, 1506–1529.
- Snyder, N. P., Whipple, K. X., Tucker, G. E., & Merritts, D. J. (2000). Landscape response to tectonic forcing: Digital elevation model analysis of stream profiles in the mendocino triple junction region, northern california. *Geological Society of America Bulletin*, 112(8), 1250–1263.
- Swarztrauber, P. N. (2003). On computing the points and weights for Gauss-Legendre quadrature. *SIAM Journal on Scientific Computing*, 24(3), 945–954.
- Szegő, G. (1939). *Orthogonal polynomials* (No. v. 23). American Mathematical Society. Retrieved from <https://books.google.com/books?id=RemVAAQBAJ>
- Talling, P. J., Stewart, M. D., Stark, C. P., Gupta, S., & Vincent, S. J. (1997). Regular spacing of drainage outlets from linear fault blocks. *Basin research*, 9(4), 275–302.
- Tarboton, D. G., Bras, R. L., & Rodriguez-Iturbe, I. (1991). On the extraction of channel networks from digital elevation data. *Hydrological Processes*, 5(1), 81–100. doi: <https://doi.org/10.1002/hyp.3360050107>
- Tucker, G., & Whipple, K. (2002). Topographic outcomes predicted by stream erosion models: Sensitivity analysis and intermodel comparison. *Journal of Geophysical Research: Solid Earth*, 107(B9), ETG–1.
- Tucker, G. E., & Bras, R. L. (1998). Hillslope processes, drainage density, and landscape morphology. *Water resources research*, 34(10), 2751–2764.
- Tucker, G. E., & Hancock, G. R. (2010). Modelling landscape evolution. *Earth Surface Processes and Landforms*, 35(1), 28–50. doi: 10.1002/esp.1952
- Van De Wiel, M. J., Coulthard, T. J., Macklin, M. G., & Lewin, J. (2007). Embedding reach-scale fluvial dynamics within the caesar cellular automaton landscape evolution model. *Geomorphology*, 90(3–4), 283–301.
- Vlase, S., Marin, M., & Öchsner, A. (2019). *Eigenvalue and eigenvector problems in applied mechanics*. Springer.
- Weinmann, P. E., & Laurenson, E. M. (1979). Approximate flood routing methods: A review. *Journal of the Hydraulics Division*, 105(12), 1521–1536.
- Whipple, K. X., & Tucker, G. E. (1999). Dynamics of the stream-power river incision model: Implications for height limits of mountain ranges, landscape response timescales, and research needs. *Journal of Geophysical Research: Solid Earth*, 104(B8), 17661–17674. doi: 10.1029/1999JB900120
- Willgoose, G., Bras, R. L., & Rodriguez-Iturbe, I. (1991). A coupled channel network growth and hillslope evolution model: 1. Theory. *Water Resources Research*, 27(7), 1671–1684.